Local Balance and Variability of Atmospheric Heat Budget over Oceans: Observation and Reanalysis-Based Estimates

SUN WONG

Jet Propulsion Laboratory, California Institute of Technology, Pasadena, California

TRISTAN S. L'ECUYER

Department of Atmospheric and Oceanic Sciences, University of Wisconsin–Madison, Madison, Wisconsin

WILLIAM S. OLSON

JCET, University of Maryland, Baltimore County, Baltimore, and NASA Goddard Space Flight Center, Greenbelt, Maryland

XIANAN JIANG

Joint Institute for Regional Earth System Science & Engineering, University of California, Los Angeles, Los Angeles, California

ERIC J. FETZER

Jet Propulsion Laboratory, California Institute of Technology, Pasadena, California

(Manuscript received 28 February 2013, in final form 9 September 2013)

ABSTRACT

The authors quantify systematic differences between modern observation- and reanalysis-based estimates of atmospheric heating rates and identify dominant variability modes over tropical oceans. Convergence of heat fluxes between the top of the atmosphere and the surface are calculated over the oceans using satellite-based radiative and sensible heat fluxes and latent heating from precipitation estimates. The convergence is then compared with column-integrated atmospheric heating based on Tropical Rainfall Measuring Mission data as well as the heating calculated using temperatures from the Atmospheric Infrared Sounder and wind fields from the Modern-Era Retrospective Analysis for Research and Applications (MERRA). Corresponding calculations using MERRA and the European Centre for Medium-Range Weather Forecasts Interim Re-Analysis heating rates and heat fluxes are also performed. The geographical patterns of atmospheric heating rates show heating regimes over the intertropical convergence zone and summertime monsoons and cooling regimes over subsidence areas in the subtropical oceans. Compared to observation-based datasets, the reanalyses have larger atmospheric heating rates in heating regimes and smaller cooling rates in cooling regimes. For the averaged heating rates over the oceans in 40°S–40°N, the observation-based datasets have net atmospheric cooling rates (from -15 to $-22 \, \mathrm{W \, m^{-2}}$) compared to the reanalyses net warming rates (5.0–5.2 $\mathrm{W \, m^{-2}}$). This discrepancy implies different pictures of atmospheric heat transport. Wavelet spectra of atmospheric heating rates show distinct maxima of variability in annual, semiannual, and/or intraseasonal time scales. In regimes where deep convection frequently occurs, variability is mainly driven by latent heating. In the subtropical subsidence areas, variability in radiative heating is comparable to that in latent heating.

1. Introduction

Remote sensing instruments on board present-day satellite platforms have measured various components of the earth's energy cycle. Retrieval (e.g., L'Ecuyer and Stephens 2003; Trenberth et al. 2009) and analysis (e.g., Dee et al. 2011; Rienecker et al. 2011; Saha et al. 2010) products are now available for studies of the global energy cycle. Among these products are the atmospheric temperature measured by Atmospheric Infrared Sounder (AIRS)/Advanced Microwave Sounding Unit (Divakarla et al. 2006; Fetzer et al. 2004, 2006; Susskind et al. 2006)

Corresponding author address: Sun Wong, MS 233-304, 4800 Oak Grove Drive, Pasadena, CA 91109.
E-mail: sun.wong@jpl.nasa.gov

on board the *Aqua* satellite (launched on 4 May 2002); diabatic heating rate profiles from sensors on board the Tropical Rainfall Measuring Mission (TRMM) (Grecu and Olson 2006; Grecu et al. 2009; L'Ecuyer and Stephens 2003, 2007; L'Ecuyer and McGarragh 2010); the National Aeronautics and Space Administration (NASA) Global Energy and Water Cycle Experiment surface radiation budget (SRB) (Fu et al. 1997; Gupta et al. 1992; Gupta et al. 2001; Pinker and Laszlo 1992); the high-frequency precipitation (*P*) syntheses such as the Global Precipitation Climatology Project (GPCP) (Huffman et al. 2001; Huffman et al. 2009); estimates of surface sensible heat fluxes (SH) from the Goddard Satellite-Based Surface Turbulent Fluxes (GSSTF) (Brunke et al. 2011; Chou et al. 2003; Shie et al. 2009) and the objectively analyzed air–sea fluxes (OAFlux; Yu and Weller 2007); and the reanalysis temperature, heating rate, and flux products such as those from the NASA Goddard Space Flight Center (GSFC) Modern-Era Retrospective Analysis for Research and Applications (MERRA) (Rienecker et al. 2011) and the European Centre for Medium-Range Weather Forecasts (ECMWF) Interim Re-Analysis (ERA-Interim) (Dee et al. 2011). Studies of energy balance have been focused mainly on the balances of the heat fluxes at the top of the atmosphere (TOA) and the surface and the inferred poleward or land–ocean heat transport (Bosilovich et al. 2011; Lin et al. 2008; Stephens et al. 2012a; Trenberth et al. 2009, 2011; Zhang et al. 2004; Zhang et al. 2006). Here we focus on the consistency between the atmospheric heating rates and the flux convergence between the TOA and the surface to identify systematic differences among the various datasets. Furthermore, we quantify the consistency among these datasets with regard to the variability at different time scales.

The atmospheric diabatic heating rates are linked to temperature *T* by the following equation (e.g., Peixoto and Oort 1992, chapter 12):

$$Q(x,y,p,t) = -\left(\frac{\partial T}{\partial t} + u\frac{\partial T}{\partial x} + v\frac{\partial T}{\partial y} + \omega\frac{\partial T}{\partial p}\right) + \frac{\kappa\omega T}{p}. \tag{1}$$

Here u, v, and ω are the horizontal and vertical wind velocities, respectively; Q is referred to as the apparent heat source (Schumacher et al. 2008; Shige et al. 2008; Wong et al. 2011b; Yanai et al. 1973) and is usually denoted as Q1 in the literature. It includes net radiative heating, latent heating, and convergence of small-scale eddy heat transport. Moreover, the integration of Q over the atmospheric column should balance the local convergence of heat flux and latent heat release in precipitation (Peixoto and Oort 1992, chapter 12),

$$\int_{p_t}^{p_s} c_p Q(x,y,p,t)\frac{dp}{g} = \Delta\text{SW}(x,y,t) + \Delta\text{LW}(x,y,t)$$
$$+ \text{SH}(x,y,t) + LP(x,y,t). \tag{2}$$

Here c_p is the heat capacity of air at constant pressure and g is the gravitational constant; ΔSW represents the local convergence of shortwave radiative flux between the top of the atmosphere and the surface (i.e., the net downward shortwave radiative flux at the top of the atmosphere minus that at the surface); ΔLW represents the local convergence of longwave radiative flux between the top of the atmosphere and the surface; SH represents the sensible heat flux from the surface; and P is the precipitation rate, which is multiplied by the water latent heat of evaporation L to give the rate of latent heat release to the atmospheric column. The integration in Eq. (2) is in pressure p from the top of the atmosphere (p_t) to the surface (p_s).

Remote sensing retrievals or reanalysis fields of temperature along with wind products from reanalyses should provide a robust measure of Q1 in the atmosphere that is consistent with independently estimated diabatic heating rates. Moreover, the vertically integrated Q1 should equal the convergence of heat fluxes between the TOA and the surface. As long as such consistency is established in the satellite observations and reanalysis products at every location on the globe, the atmospheric branch of the energy cycle can be described as "balanced." Systematic differences between datasets that result in imbalance in the energy budget will be identified in the present study.

In this study, we will investigate three estimates of Q1: 1) the diabatic heating profiles based on the TRMM, 2) the remotely sounded T from AIRS used together with the MERRA wind fields to estimate global patterns of diabatic heating rates, and 3) the diabatic heating profiles of the MERRA and ERA-Interim. Comparison of the column integrals of these diabatic heating rates to the convergence of independent estimates/measurements of heat fluxes between the TOA and the surface provides a means to investigate balance between different satellite-based heating datasets. The estimates of heat fluxes include the SRB radiative fluxes, GSSTF, version 2c (GSSTF2c), or OAFlux sensible heat flux, and GPCP 1° daily (1DD) precipitation rates, as well as the MERRA and ERA-Interim heat fluxes at the TOA and the surface. Variability of the estimated and reanalysis column heating rates as well as the observed and reanalysis heat flux convergences will be assessed individually using maps of seasonal averages and wavelet analyses. Parallel analyses of the local balance of atmospheric water cycle are described in Wong et al. (2011a).

2. Data

Diabatic heating rates were directly estimated based on the TRMM data, referred to as "trained" radiometer heating (TRAIN) Q1. TRAIN Q1 is a combination of estimates of latent and eddy sensible heating rates, referred to as Q1R, in and outside of precipitation regions (Grecu and Olson 2006; Grecu et al. 2009) and radiative heating rates based on the Hydrological Cycle and the Earth Radiation Budget (HERB) algorithm, referred to as QR (L'Ecuyer and Stephens 2003, 2007; L'Ecuyer and McGarragh 2010). The TRAIN Q1 data are available over oceans between about 40°N and 40°S latitude. In the following, we briefly describe the algorithms involved in the dataset. Please refer to the above references for detailed information.

The QR profiles were estimated by a broadband radiative transfer model with inputs of ice cloud properties from Visible and Infrared Scanner (VIRS) (Cooper et al. 2003), liquid cloud properties, precipitation profiles, sea surface temperature, water vapor retrievals from the TRMM Microwave Imager (TMI) (Greenwald et al. 1993), and vertical profiles of temperature and humidity from National Centers for Environmental Prediction (Kalnay et al. 1996) reanalyses. To obtain Q1R profiles in precipitation regions, a large database of heating profile–brightness temperature pairs is first created from TRMM precipitation radar (PR) (Grecu and Olson 2006) estimated precipitation/heating profiles and collocated TMI observed brightness temperatures. Precipitation radar Q1R profile estimates are obtained by matching cloud-resolving model simulated profiles to PR-derived profiles that have similar convective–stratiform classification, echo top height, and surface rain rate characteristics, as described in Grecu et al. (2009). Then, in applications of the heating algorithm to any set of observed TMI brightness temperatures, the database is scanned to find Q1R profiles associated with a consistent set of database brightness temperatures, and a Bayesian composite Q1R profile estimate is constructed from these radiometrically consistent profiles (Grecu and Olson 2006). Outside regions of precipitation, Q1R profiles are estimated such that the diabatic heating rates Q1 balance the large-scale vertical advection of potential temperature in an idealized convective boundary layer. TRAIN Q1 is the sum of QR and Q1R and gridded at 0.5° × 0.5° resolution. The estimates are averaged over 5° latitude × 10° longitude grid boxes and interpolated onto the AIRS standard pressure levels for comparison with the heating rates calculated from the AIRS temperature and MERRA wind fields as described below. We simply refer the column integral of the TRAIN Q1 as TRAIN Q1.

Here Q1 can also be estimated from a combination of remotely sounded T profiles and reanalysis winds using Eq. (1). We use the AIRS level 3 (L3) version 5 temperature product at 1° × 1° horizontal resolution (Olsen et al. 2007) and the MERRA (version 5.2) wind field product. Equation (1) is applied to daily data. Since AIRS makes tropical measurements around 0130 and 1330 local time, the daily averaged T within each 1° × 1° grid is computed as the average of the two measurements at the two local times. There are two sampling issues that need to be addressed. The first regards the lack of sampling in cloudy areas, complicating the calculation of temperature gradients at nominal sensor resolution, so AIRS daily T are averaged onto 5° latitude × 10° longitude grid boxes that provide acceptable spatial coverage of the T gradients needed in the calculation of Q1 over the globe. The second issue is cloud-induced sampling biases related to the poor AIRS sampling in cloudy areas. Cloud-induced temperature sampling biases depend on the cloud types (Yue et al. 2013). For most types of clouds, the biases are about 1 K. In heavily precipitating clouds in the tropics and middle latitudes, the cold biases can be as high as 5 K throughout the middle to lower troposphere by comparison to collocated radiosonde data. In regions where deep convection frequently occurs, adiabatic heating [the last term in Eq. (1)], which is proportional to T, dominates the estimate of Q1. The cold biases in AIRS T in these regions cause underestimation of atmospheric heating rates compared to the reanalyses, as discussed in section 3.

MERRA uses the Goddard Earth Observing System Data Assimilation System version 5 (GEOS-5) (Rienecker et al. 2008; Rienecker et al. 2011) to assimilate observations, including AIRS radiance data, for the analysis. The 3-hourly instantaneous MERRA winds are averaged daily onto the same 5° × 10° grid boxes as used for AIRS. The MERRA winds are interpolated or averaged from the 42 pressure levels to the 24 AIRS standard pressure levels for T. After these fields are consistently processed on a common grid, the rhs of Eq. (1) can be calculated on 5° latitude × 10° longitude grids, where the gradients are computed by finite differencing in spherical coordinates. We chose p_t in Eq. (2) to be 70 hPa, the highest level where the TRAIN Q1 heating rates are estimated. The contribution to total heating rates from the atmosphere above this altitude is at least one order of magnitude smaller than from the atmosphere below and is neglected in this work. Hereafter the column integral of Q1 in Eq. (2) that uses AIRS T and MERRA winds is referred to as AIRS/MERRA Q1. We have used the MERRA T and winds to mimic the real-world situation and performed tests of sensitivity of the biases, from the actual MERRA diabatic heating rates, to

different combinations of the sampled T and winds and spatial averaging for the calculations. The above described method provides the most accurate approximation to the actual MERRA diabatic heating rates, given the twice per day sampling frequency and large size ($5° \times 10°$) grid boxes. Using the daily averaged wind fields, instead of the wind field snapshots that are simultaneous to AIRS measurements, is critical in providing more accurate daily averaged heating rates. We have also used ERA-Interim winds, instead of MERRA winds, and found that they yield a Q1 very similar to that of AIRS/MERRA Q1.

To compute the heat flux convergence between the TOA and the surface, we apply the SRB shortwave (SW) and longwave (LW) radiative fluxes (Fu et al. 1997; Gupta et al. 1992; Gupta et al. 2001; Pinker and Laszlo 1992; Stackhouse et al. 2011). In this study, the radiative fluxes are from the SW and LW quality-check algorithm (Gupta et al. 1992, 2001). The daily and monthly mean of the flux data have a general bias of $\sim 4\,\mathrm{W\,m}^{-2}$. The data are derived on a $1° \times 1°$ resolution grid, and we average them onto $5° \times 10°$ grid boxes for comparison with other data.

The precipitation P in Eq. (2) is obtained from the GPCP 1DD (version 1.2) data product, daily precipitation syntheses at $1° \times 1°$ resolution. It is based on the GPCP version 2.2 satellite–gauge product, which merges global precipitation-gauge analyses with precipitation retrievals from satellites including Special Sensor Microwave Imager and Image/Sounder (SSM/I and SSM/IS), Television and Infrared Observation Satellite (TIROS) Operational Vertical Sounder (TOVS), AIRS, and others (Huffman et al. 2001; Huffman et al. 2009 and references therein). In this study, the GPCP 1DD P fields are averaged daily on $5° \times 10°$ grid boxes to facilitate comparison to other data and simply referred to as GPCP.

The SH term in Eq. (2) is obtained from two data sources. First, the GSSTF2c dataset 1 daily sensible heat flux estimates are based on a bulk flux model with inputs of SSM/I retrievals of 10-m wind speeds as well as sea surface temperature, 2-m air temperature, and sea level pressure from National Centers for Environmental Prediction–Department of Energy (NCEP–DOE) Reanalysis-2 (Chou et al. 2003; Shie et al. 2009; Shie 2011; Shie et al. 2011). Second, the OAFlux is derived from a variational objective analysis applied to meteorological data from national weather prediction centers to provide inputs for a bulk flux algorithm to estimate sensible heat fluxes. The meteorological data for their variational analysis include surface meteorology from the NCEP–DOE and the ECMWF operational forecast analysis [40-yr ECMWF Re-Analysis (ERA-40)]

and satellite retrievals of wind from the Quick Scatterometer (QuikSCAT) and surface temperature from the Advanced Very High Resolution Radiometer (AVHRR), TMI, and Advanced Microwave Scanning Radiometer for Earth Observing System (EOS) (AMSR-E) (Yu and Weller 2007). Both daily sensible heat flux datasets (GSSTF2c and OAFlux) are reported at $1° \times 1°$ resolution and then averaged over $5° \times 10°$ grid boxes for comparison with other data.

The SRB radiative heat fluxes at the TOA and the surface, the GSSTF2c SH, and the GPCP precipitation will be inputs of the rhs of Eq. (2), referred to as the synthetic flux convergence (FLUX CONV). Their seasonal averages and variability will be compared with those of TRAIN Q1 and AIRS/MERRA Q1.

While MERRA and ERA-Interim assimilate AIRS radiance data, it provides fields of T, even in cloudy areas. Thus, we also calculate total Q1 directly from the MERRA and ERA-Interim heat budgets (i.e., from the dynamical T tendencies), referred to as MERRA Q1 and ERA Q1. The MERRA and ERA Q1 are averaged onto $5° \times 10°$ grid boxes from their original resolutions for comparison with other data. Moreover, the radiative and sensible heat flux convergences as well as the estimated latent heating of the atmosphere from MERRA and ERA-Interim precipitations are also examined, referred to as the MERRA FLUX CONV and ERA FLUX CONV. Bosilovich et al. (2011) documented details of the water and energy cycles in MERRA. While they focused on energy balances at the TOA and the surface individually and how the assimilation system is sensitive to perturbations in the observation record, in the present study the balance of atmospheric heating with the convergence of the heat fluxes between the TOA and the surface is tested.

While the reanalysis Q1 and FLUX CONV are simply model forecasts, AIRS/MERRA Q1, TRAIN Q1, and the synthetic FLUX CONV are all estimates calculated using different data resources. Table 1 summarizes the acronyms of the data resources that are used for these estimates.

3. Results

a. Fluxes at the TOA and the surface

Climatological averages of the HERB net downward radiative fluxes at the TOA are shown in Fig. 1 for boreal winter [December–February (DJF), Fig. 1a] and summer [June–August (JJA), Fig. 1b]. Also shown are the differences of the SRB (Figs. 1c,d), MERRA (Figs. 1e,f), and ERA-Interim (Figs. 1g,h) fluxes from the HERB fluxes. The uncertainties of HERB TOA radiative fluxes at different spatial scales have been estimated (L'Ecuyer and

TABLE 1. Summary of acronyms of the data resources used to calculate AIRS/MERRA Q1, TRAIN Q1, and synthetic FLUX CONV discussed in this study.

	Dynamic	Radiation	Latent heat	Sensible/turbulent
AIRS/MERRA Q1	AIRS T and MERRA winds	—	—	—
TRAIN Q1	—	HERB QR	TRAIN Q1R	Estimated (see text)
FLUX CONV	—	SRB	GPCP 1DD	GSSTF2c

McGarragh 2010). We use the 1σ uncertainty of the HERB TOA fluxes for $5° \times 5°$ grid box size (close to our gridbox size) as contour interval to plot Figs. 1c–h to indicate the significance of systematic differences between the datasets.

All datasets show maxima in the summer hemisphere over the subtropical oceans. The net downward flux is largest in the HERB (Figs. 1a,b) dataset and smallest in the reanalyses (Figs. 1e–h). Presented in Table 2 are the net downward radiative fluxes averaged over the oceans in 40°S–40°N for the winter and summer seasons in 2004–07. The averaged fluxes are further decomposed into net downward SW fluxes and outgoing longwave radiation (OLR). The reanalyses have the largest OLR that contributes to its smallest net downward radiative flux, and the HERB has the largest net downward shortwave flux as well as the smallest OLR, resulting in its largest net downward radiative flux.

The maxima of net downward fluxes at the surface are also located in the summertime subtropics (Fig. 2). The differences from HERB are plotted with contour interval representing 1σ uncertainty in the HERB surface fluxes (L'Ecuyer and McGarragh 2010). HERB (Figs. 2a,b) has the largest surface net downward radiative fluxes, while the reanalyses (Figs. 2e,f) have the smallest surface fluxes. This is because HERB has the largest net downward shortwave radiation and the smallest longwave cooling at the surface (Table 3). The reanalyses largest longwave cooling contribute to their smallest net downward surface radiative fluxes. From Figs. 2c–h, we see that the SRB and the reanalyses have much smaller net downward radiative fluxes than for HERB over regions with deep convective clouds, such as the Asian and American monsoon regions during boreal summer and the tropical western Pacific during winter. This implies that the cloud forcing at the surface is smaller in HERB than in the SRB and the reanalyses.

The radiative heating of the atmosphere (Fig. 3) is the difference between the net downward radiative fluxes at the TOA and the surface. In the clear-sky oceanic area, the atmosphere is cooled by radiation to space. In the regions with large cloud cover, this clear-sky cooling is mitigated by the cloud warming effect. The stronger cloud warming in MERRA is evident in Figs. 3e,f over the Asian and American monsoon regions during summer

and the tropical western Pacific, where the cloud forcing in HERB is relatively weaker. By comparing the annually averaged longwave cloud forcing at the TOA in MERRA to that in the SRB, Bosilovich et al. (2011) has demonstrated that MERRA has stronger cloud forcing than the SRB over the tropical western Pacific, Indian Ocean, and Central America.

We also see in Fig. 3 that HERB (used in TRAIN Q1) has stronger cooling in the atmosphere over the regions with extensive low-level clouds, such as the subsidence area over subtropical oceans, compared to the reanalyses (Figs. 3e–h). In these regions, downward longwave radiation is larger than that in the tropical regions with deep convective clouds (Stephens et al. 2012b), and measurement of cloud base is essential in determining the cloud radiative forcing. HERB is based on the TRMM microwave sensor (TMI), which is sensitive in detecting low cloud at night and provides a larger downward longwave radiative flux and, hence, larger atmospheric cooling in these regions. The net downward longwave radiative fluxes of HERB averaged over the oceanic surface in 40°S–40°N (Table 3) is larger than those of the reanalyses by about $10–18 \, \mathrm{W \, m^{-2}}$. Stephens et al. (2012b) also reported a systematic bias of $\sim 10 \, \mathrm{W \, m^{-2}}$ in downward longwave radiative flux between the satellite synthesis product and reanalyses, although their results are for global averages over the ocean.

The first column in Table 4 includes the radiative heating rates in the atmosphere averaged over the oceans in 40°S–40°N. HERB has the largest annually averaged radiative cooling rates in the atmosphere ($-122 \, \mathrm{W \, m^{-2}}$), while the atmospheric radiative cooling rates in MERRA ($-114 \, \mathrm{W \, m^{-2}}$) and ERA-Interim ($-116 \, \mathrm{W \, m^{-2}}$) are close to the SRB value (about $-113 \, \mathrm{W \, m^{-2}}$).

The atmosphere is heated from the surface by sensible heat flux. In Fig. 4 we compare the sensible heat fluxes from GSSTF2c, OAFlux, MERRA, and ERA-Interim for both boreal winter and summer in 2004–07. All datasets show that sensible heat fluxes are largest in area where cold wintertime continental air masses move over warm ocean currents to the east of the continents. OAFlux (Fig. 4c) has the largest sensible heat fluxes in Northern Hemisphere during the boreal winter, while MERRA (Fig. 4e) has the smallest fluxes in this season. In the Southern Hemisphere, OAFlux (Fig. 4d), MERRA
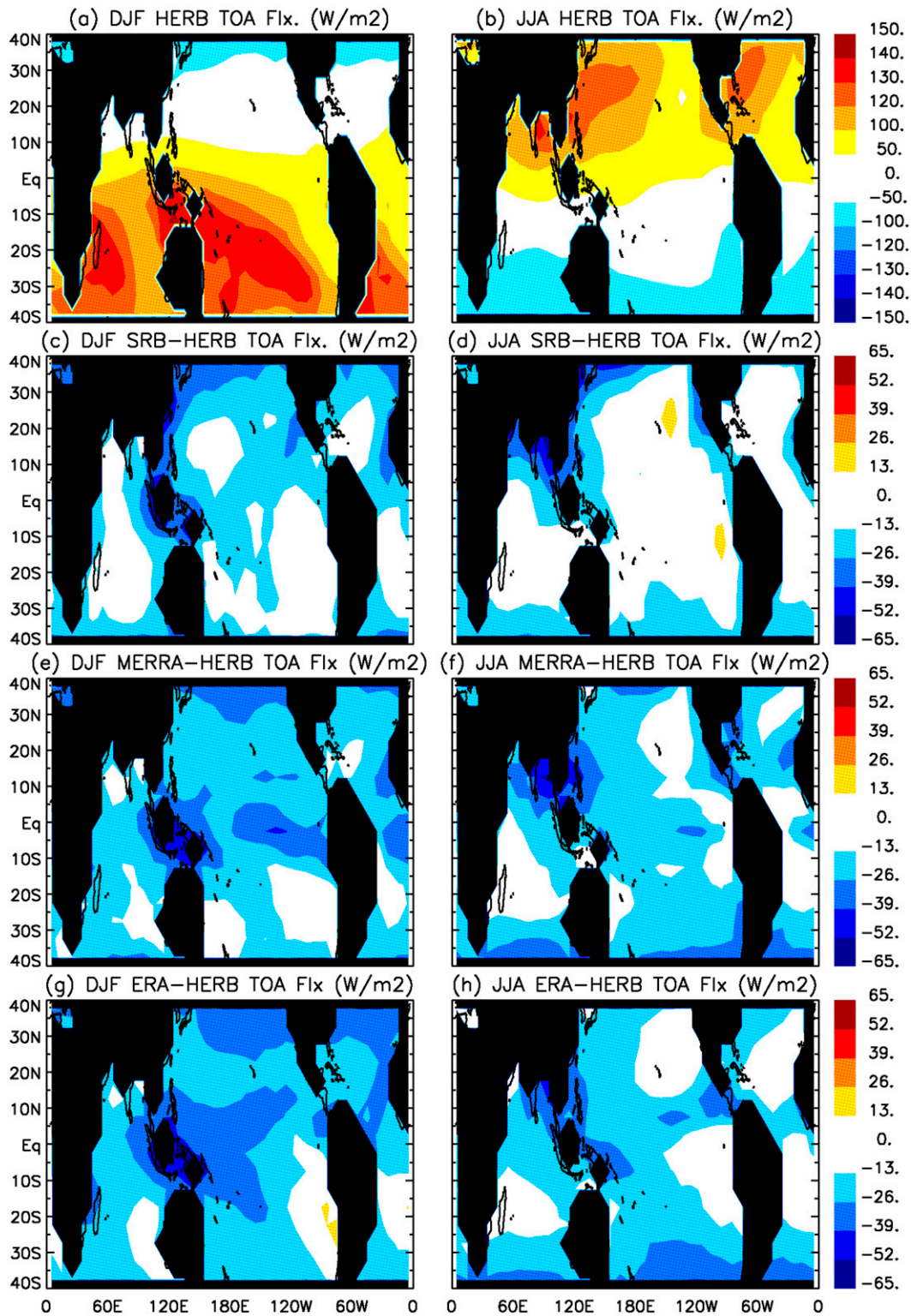
FIG. 1. (a),(b) The HERB net downward radiative fluxes (W m^{-2}) at the TOA. Differences, from the HERB, in the TOA net downward radiative fluxes of (c),(d) SRB; (e),(f) MERRA; and (g),(h) ERA-Interim: (left) the seasonal averages of the fluxes/flux differences for DJF in 2004–07 and (right) the averages for JJA in the same years. For (c)–(h), contour interval is the 1σ uncertainty of the HERB radiative fluxes at TOA. The black area indicates regions with land cover greater than 50%.

TABLE 2. Seasonal-mean net downward shortwave fluxes and outgoing longwave fluxes ($W m^{-2}$) at the TOA averaged over the oceans (land cover < 50%) in 40°S–40°N for 2004–07.

	Net SW		OLR		Net downward	
	DJF	JJA	DJF	JJA	DJF	JJA
HERB	317.5	282.8	249.8	251.5	67.7	31.3
SRB	306.9	277.3	255.4	257.0	51.4	20.3
MERRA	310.0	271.8	262.9	258.7	47.1	13.1
ERA-Interim	309.7	277.2	263.4	262.8	46.3	14.4

(Fig. 4f), and ERA-Interim (Fig. 4h) have comparable sensible heat fluxes during the austral winter, while GSSTF2c (Fig. 4b) has the smallest fluxes. The annually averaged sensible heat fluxes over the oceans in 40°S–40°N from different datasets are shown in the third column of Table 4. The MERRA and OAFlux have comparable values of (10–13 $W m^{-2}$), while the GSSTF2c value is slightly smaller (~8 $W m^{-2}$).

Brunke et al. (2011) evaluated several sensible heat flux products with respect to in situ measurements and found that GSSTF tends to underestimate sensible heat fluxes more than MERRA and OAFlux when compared to in situ measured data. Note that in TRAIN Q1 the sensible heating is represented as the turbulent heating that, along with any latent heating and radiative cooling in the convective boundary layer, compensates for large-scale subsidence warming. However, this crudely estimated turbulent heating in TRAIN Q1 is much smaller than the sensible heating estimates shown in Fig. 4. In the following, we will mainly use the GSSTF2c sensible heat flux for our calculations of FLUX CONV, while the results that use OAFlux data are discussed when necessary and listed in Table 4.

b. Heating in the atmosphere

As the atmosphere is cooled by radiation, it is heated by latent heat release during precipitation processes. Latent heat is transferred from the surface to the atmosphere by evaporation of water. The evaporated water vapor is transported, and the latent heat is released into the atmosphere where precipitation occurs. The balance of the global hydrological cycle (e.g., Trenberth et al. 2011; Wong et al. 2011a) guarantees that the transfer of latent heat energy is equal between globally averaged evaporation and precipitation. However, since only heating of the atmosphere over oceans between 40°S and 40°N is considered in this study, a balance between surface evaporation and precipitation is not expected. To focus on the latent heat release in the atmosphere, we investigate the precipitation rather than the surface latent heat flux.

Figure 5 shows the atmospheric latent heating rate climatologies calculated using TRAIN Q1R for both boreal winter and summer in 2004–07 and the differences of the latent heating rate climatologies inferred from GPCP 1DD, MERRA, and ERA-Interim precipitation products from the TRAIN Q1R climatologies. As there is no available uncertainty estimate of TRAIN Q1R, for Figs. 5–7, we simply use the 1σ uncertainty of the TRAIN QR for the contour intervals in the plots of differences. The datasets all capture the basic precipitation features: the intertropical convergence zone (ITCZ); large precipitation in the tropical western Pacific, the Indian, East Asian, and American summer monsoons; and the wintertime extratropical storm tracks. The latent heating is stronger in MERRA (Figs. 5e,f) over the tropical ocean compared to other datasets, consistent with previous results (Bosilovich et al. 2011; Trenberth et al. 2011; Wong et al. 2011a) that MERRA produces larger tropical precipitation compared to the GPCP 1DD datasets. In the ITCZ over the tropical eastern Pacific (about 120°–140°W), TRAIN Q1R (Figs. 5a,b) has stronger latent heating than GPCP and the reanalyses. The annually averaged atmospheric latent heating rates over the oceans in 40°S–40°N for TRAIN Q1R and GPCP 1DD (the second column in Table 4) are comparable (~88–90 $W m^{-2}$). The MERRA and ERA-Interim precipitations provide a larger averaged atmospheric latent heating (~100 $W m^{-2}$) compared to the observation-based datasets. The GSSTF2c surface latent heat flux product has an average of about 120.9 $W m^{-2}$ over the oceans in 40°S–40°N because there is an excess of precipitation relative to evaporation over land (Trenberth et al. 2011), which is not included in our calculation.

The net column atmospheric heating from TRAIN Q1 and the differences of AIRS/MERRA, MERRA, and ERA-Interim heating budgets from TRAIN Q1 are shown in Fig. 6. Strong atmospheric heating is seen in regions of high precipitation rates. These include the ITCZ, the summertime monsoon regions, the tropical western Pacific, and the extratropical storm tracks. The cooling of the atmosphere mainly occurs over the eastern part of subtropical oceans, where radiative cooling dominates, and at the higher latitudes not considered in this study. Compared to TRAIN Q1, AIRS/MERRA Q1 (Figs. 6c,d) is smaller over the tropical western Pacific during boreal winter but larger in the summertime monsoon area. Compared to the reanalyses, the cold biases in AIRS temperatures result in the smaller AIRS/MERRA Q1 in these regions of frequent deep convection. The atmospheric heating in the boreal summer monsoon areas is the strongest in the reanalyses (Figs. 6e–h) because of the local stronger latent heating compared to other datasets (Fig. 5).
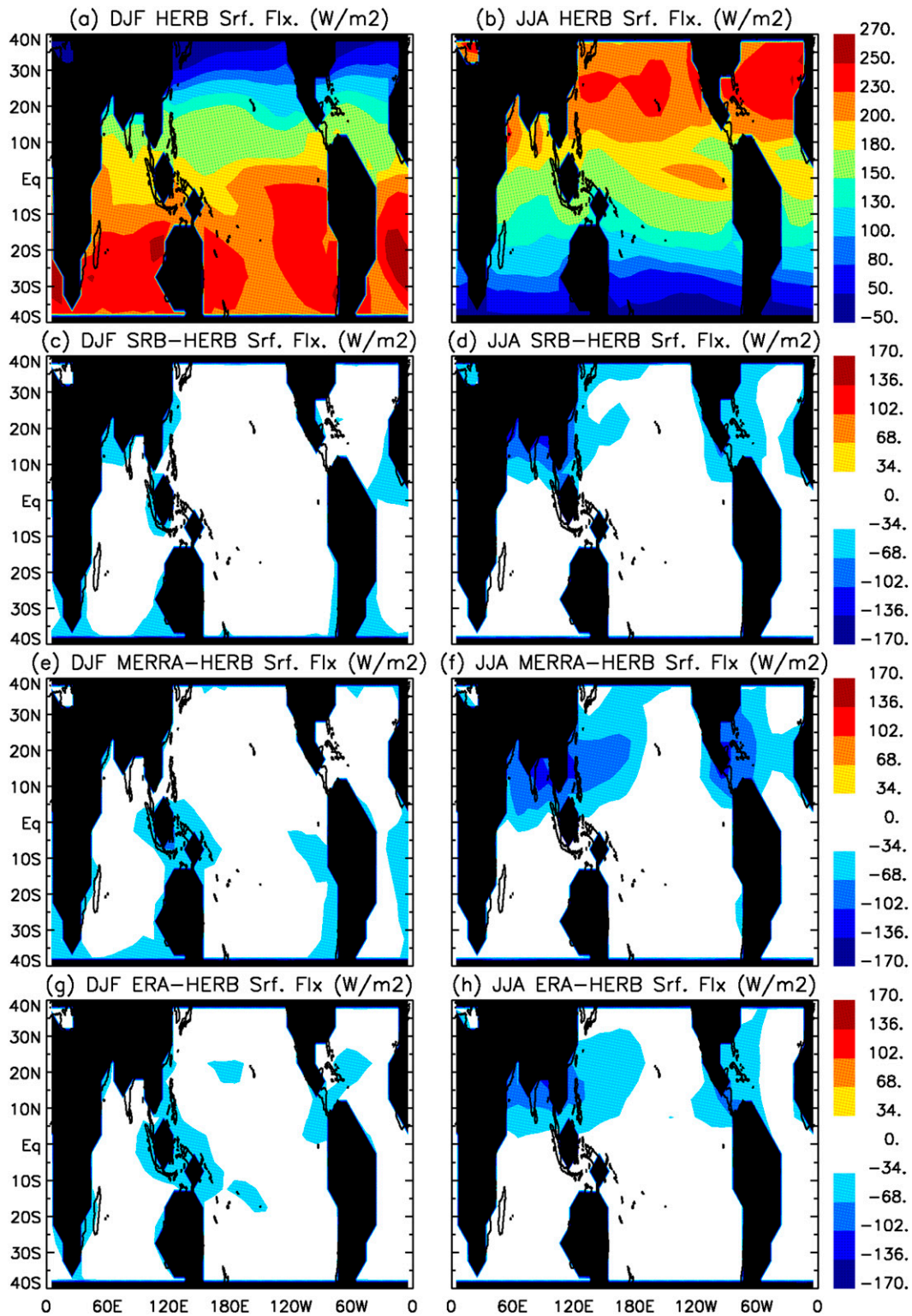
FIG. 2. As in Fig. 1, but at the surface.

TABLE 3. As in Table 2, but at the surface.

	Net SW		Net LW		Net downward	
	DJF	JJA	DJF	JJA	DJF	JJA
HERB	233.5	206.2	−47.9	−46.2	185.6	160.0
SRB	214.3	189.3	−51.4	−49.5	162.7	139.8
MERRA	224.1	191.6	−65.2	−62.7	158.9	128.9
ERA-Interim	216.2	190.2	−57.1	−55.3	159.1	134.9

The column atmospheric heating rates in Fig. 6 can be compared with the synthetic heat flux convergence between the TOA and the surface plus latent heating rates according to Eq. (2). Both boreal winter and summer differences of the FLUX CONV, MERRA, and ERA-Interim heat flux convergences from the corresponding TRAIN Q1 climatologies are shown in Fig. 7. As expected, the reanalysis heat flux convergences generally agree with the reanalysis column atmospheric heating shown in Figs. 6e–h. The detailed differences between the reanalysis column-integrated heating rates and heat flux convergences are mainly caused by the analysis increments when the assimilation systems correct the simulated temperature according to observational inputs. In contrast, TRAIN Q1 and FLUX CONV do not have to balance since the observation-based estimates are independently computed.

While the general geographical patterns in Figs. 6 and 7 are consistent, regional differences indicate where inconsistency of energy budget may occur among the different datasets. In the tropics, MERRA (Figs. 6e,f and 7c,d) has the strongest heating rates over regions of heavy precipitation, consistent with its larger precipitation compared to GPCP. In the eastern part of subtropical oceans, TRAIN Q1 has the strongest cooling rates. In the extratropics, AIRS/MERRA and the reanalyses have stronger heating rates in the boreal winter storm tracks compared to FLUX CONV, while TRAIN Q1 has the weakest heating rates in the storm tracks.

The zonally averaged atmospheric heating rates or flux convergences over the oceans are shown in Fig. 8 for the different datasets. The datasets show similar latitudinal and seasonal variations. During boreal winter (Fig. 8a), the discrepancy between the reanalyses and the observation-based estimates is mainly located in the tropics, owing to the larger reanalysis atmospheric heating rates over the tropical western Pacific (Figs. 6 and 7). During boreal summer (Fig. 8b), the discrepancy is mainly located over 10°–35°N, with the reanalyses having the largest heating rates and TRAIN Q1 having the smallest heating rates. This is due to the larger monsoon-related heating rates in the reanalyses and the larger cooling rates in TRAIN Q1 over subtropical oceans (Figs. 6 and 7). The discrepancy between the

reanalyses and the observation-based estimates is still evident after the annual averaging is taken (Fig. 8c).

The global averaged atmospheric heating rates over the oceans in 40°S–40°N for 2004–07 are listed in the last column of Table 4. The TRAIN Q1, AIRS/MERRA, and FLUX CONV have the averaged heating rates ranging from −15 to −22 W m^{-2}. TRAIN Q1 has the smallest atmospheric heating rates because of its larger radiative cooling rates. The FLUX CONV averaged heating rates are the largest (from −15 to −17 W m^{-2}) among the observation-based syntheses. Notice that the latent heating rates calculated from GPCP precipitation and in TRAIN Q1R are about 12 W m^{-2} smaller than those from the reanalyses. The MERRA and ERA-Interim flux convergences over the oceans in 40°S–40°N are slightly less than zero (from −0.2 to −0.9 W m^{-2}). The analysis increments in the reanalyses bring their net heating over the oceans to positive values.

The discrepancy between the reanalysis atmospheric heating rates (~5.2 W m^{-2}) and the mean observation-based estimates (−18.9 W m^{-2}) is about 24 W m^{-2} over the tropical oceans, much larger than the 1σ spread (2.6 W m^{-2}) of the observation-based estimates. One main contribution of the discrepancy is from the large tropical latent heating in the reanalyses. It is reported that the TRMM or microwave-based sensors may underestimate the light precipitation (Behrangi et al. 2012; Berg et al. 2010). However, such underestimation mainly dominates in areas of frequent light precipitation (i.e., subtropical subsidence areas), and it is still an open question how much this missing light precipitation contributes to the latent heating rates in area of frequent deep convection.

c. Wavelet spectra of regional heating budgets

To further quantify the sources of variability in the heating rates and the different flux convergences, we perform wavelet analyses on regionally averaged time series of heating rates. The column-integrated heating rate and heat flux convergence fields are averaged over chosen regions that are energetically diverse (Fig. 9), and the resultant time series are transformed by the Morlet wavelet (Farge 1992). In Fig. 9, regions a, b, and d are along the ITCZ, and region c is over the subtropical ocean. The wavelet spectra for diabatic heating rates and flux convergences for these regions are shown in Figs. 10–13. We also show in the figures the wavelet spectra of the radiative and latent heating portions in the TRAIN, MERRA and ERA Q1, and FLUX CONV estimates. For FLUX CONV, the radiative heating portion is the SRB shortwave and longwave radiative flux convergence between the TOA and the surface and the latent heating portion is proportional to GPCP 1DD precipitation.
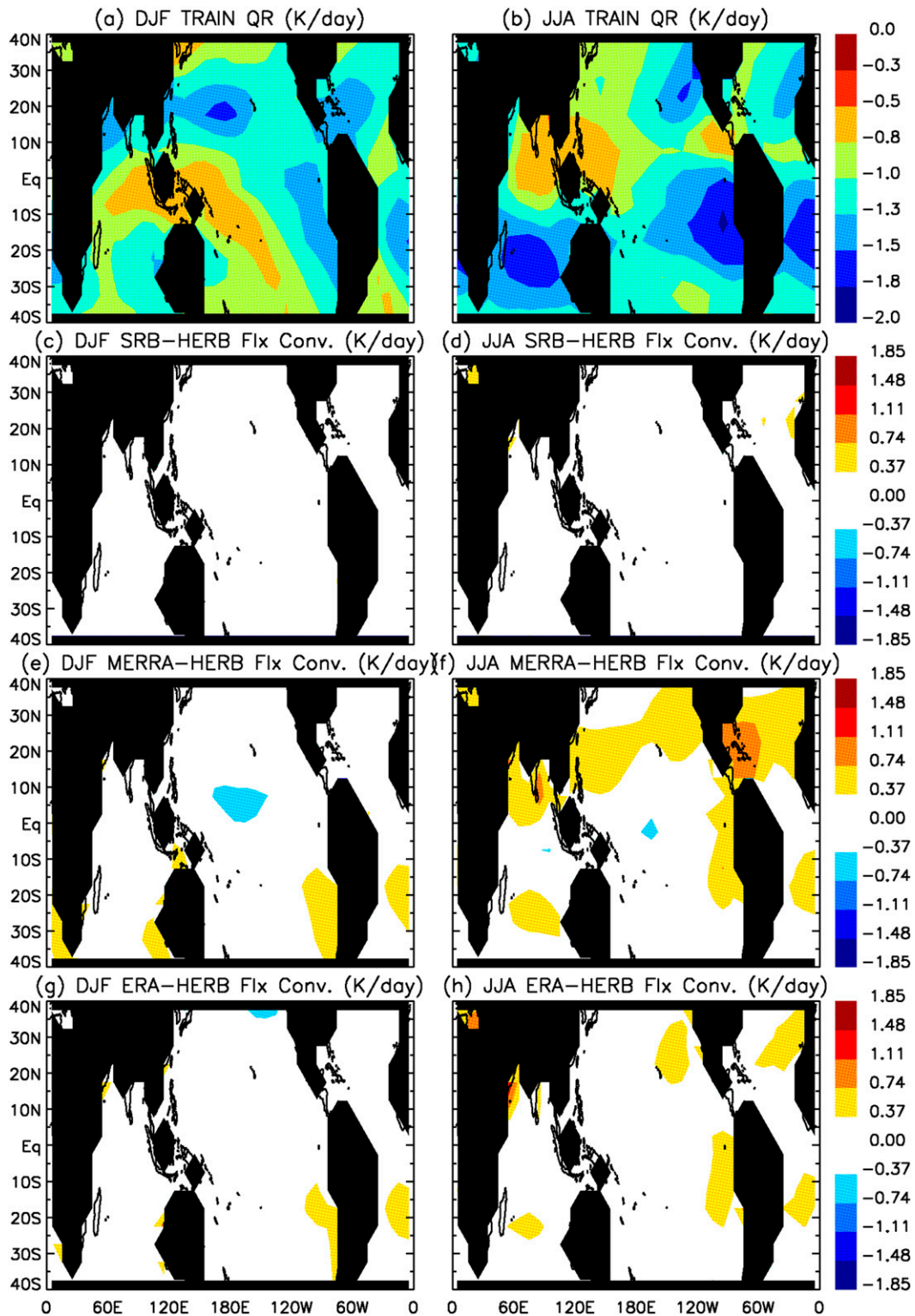
FIG. 3. (a),(b) Column-integrated atmospheric radiative heating rates of TRAIN QR. Differences, from the TRAIN QR, in the convergence of radiative fluxes between the TOA and the surface calculated for (c),(d) SRB; (e),(f) MERRA; and (g),(h) ERA-Interim: (left) the seasonal averages for DJF in 2004–07 and (right) the averages for JJA for the same years. For (c)–(h), the contour interval is the 1σ uncertainty of the TRAIN QR. The units are converted to kelvin per day by assuming an atmospheric layer thickness of 70–1000 hPa. The black area shows regions with missing data or with land cover greater than 50%.

TABLE 4. Annual-mean atmospheric diabatic heating budgets ($W\,m^{-2}$) calculated from different datasets over the oceans (land cover less than 50%) in 40°S–40°N for 2004–07. One can divide the numbers by 110.2 to convert them into kelvin per day.

	Radiation	Latent heat	Sensible/turbulent heat	Analysis increment[a]	Total
TRAIN Q1	−122.1	89.9	10.2[b]	—	−22.0
Flux convergence from syntheses	−113.9	87.9	7.9 (GSSTF2c)	—	−18.1
AIRS/MERRA Q1	—	—	10.1 (OAFlux)	—	−15.8
MERRA Q1	−114.1	100.3	—	8.3	−19.8
MERRA flux convergence	−112.6	99.4	10.7[c]	—	5.2
ERA Q1	—	—	13.0	—	−0.2
ERA flux convergence	−116.1	100.1	—	—	5.0
	—	—	15.0	—	−0.9

[a] Analysis increment is the correction in temperature in the MERRA when assimilated with observations used for the assimilation system.
[b] TRAIN Q1, turbulent heating is estimated together with the latent heating to compensate the large-scale vertical motion.
[c] This is the sum of heating rates from turbulent heating, gravity wave drag, and surface friction reported in the MERRA heat budgets.

Over the tropical Indian Ocean, there are three modes of variability in total heating rates at annual, semiannual, and intraseasonal (~30–90 days) time scales (Fig. 10, top). The timings of the peaks in semiannual and intraseasonal variations are consistent among different estimates, although the amplitudes of the variations differ among different estimates. The three-mode variability is also evident in the wavelet spectra of radiative heating rates (Fig. 10, middle). TRAIN QR, MERRA, and ERA radiative heating rates have qualitatively consistent wavelet spectra patterns. The SRB flux convergence has much weaker semiannual variation, but its intraseasonal variations are similar to the other three estimates. The variability in latent heating rates (Fig. 10, bottom) is about 3–4 times larger than that in radiative heating rates and dominates the variability of the total heating rates.

The tropical western Pacific has the largest variability in total heating rates among all regions. The annual and intraseasonal variations of the heating rates are significant in all heating rate estimates (Fig. 11, top). The timing of the intraseasonal variations is consistent among different estimates, although the amplitudes differ among the estimates, with AIRS/MERRA having the smallest amplitude at the intraseasonal time-scale variation. For the annual variability, MERRA Q1 has the largest amplitude, while TRAIN Q1 has the smallest. The radiative heating has a clear signal of annual variation (Fig. 11, middle), with the MERRA Q1 having the largest annual variation amplitude than the other estimates. The pattern of the spectra in total heating rates is again dominated by the variation in latent heating, which is about two times larger than the variation in radiative heating (Fig. 11, bottom).

In other regions along the ITCZ (e.g., the tropical eastern Pacific near the west coast of Central America and the tropical South Pacific east to New Guinea), where latent heating dominates over the clear-sky radiative cooling in

climatology, wavelet spectra patterns in diabatic heatings (not shown) exhibit similar characteristics to those in the west Pacific. In these regions, annual variation is the dominant variability mode, and variations in latent heating are always much larger than those in radiative heating.

The subtropical northeastern Pacific is a region where radiative cooling dominates over latent heating in the climatology of the atmospheric energy budget (Figs. 6 and 7). The total heating rates have significant variations at the annual, semiannual, and intraseasonal time scales (Fig. 12, top). For the annual variation, AIRS/MERRA has the smallest amplitude while TRAIN Q1 has the largest amplitude. Again, the timing of the intraseasonal variation is consistent among different estimates. The variations in radiative heating are mainly at the annual and semiannual time scales (Fig. 12, middle), and the variations in latent heating occur at all the annual, semiannual, and intraseasonal time scales (Fig. 12, bottom). Over this region, the annual variation in radiative heating (1.5–1.8 $K\,day^{-1}$) is larger than the annual variation in latent heating (0.6–1.4 $K\,day^{-1}$). However, variations of latent heating over this region are still important at semiannual and intraseasonal time scales. For the semiannual variation, the latent heating is comparable in amplitude (0.3–0.8 $K\,day^{-1}$) to the radiative heating (0.3–0.6 $K\,day^{-1}$; Fig. 12, middle and bottom). The intraseasonal variability is significant in boreal winter and is mainly caused by the variation in latent heating (Fig. 12, bottom).

Wavelet spectra of heating rates in subtropical oceans (e.g., south Indian Ocean and southeast Pacific off the coast of South America, not shown), where radiative cooling dominates the heating rate climatology, exhibit similar characteristics to those over the subtropical northeastern Pacific. Variations of radiative heating rates over these regions are comparable to variations of latent
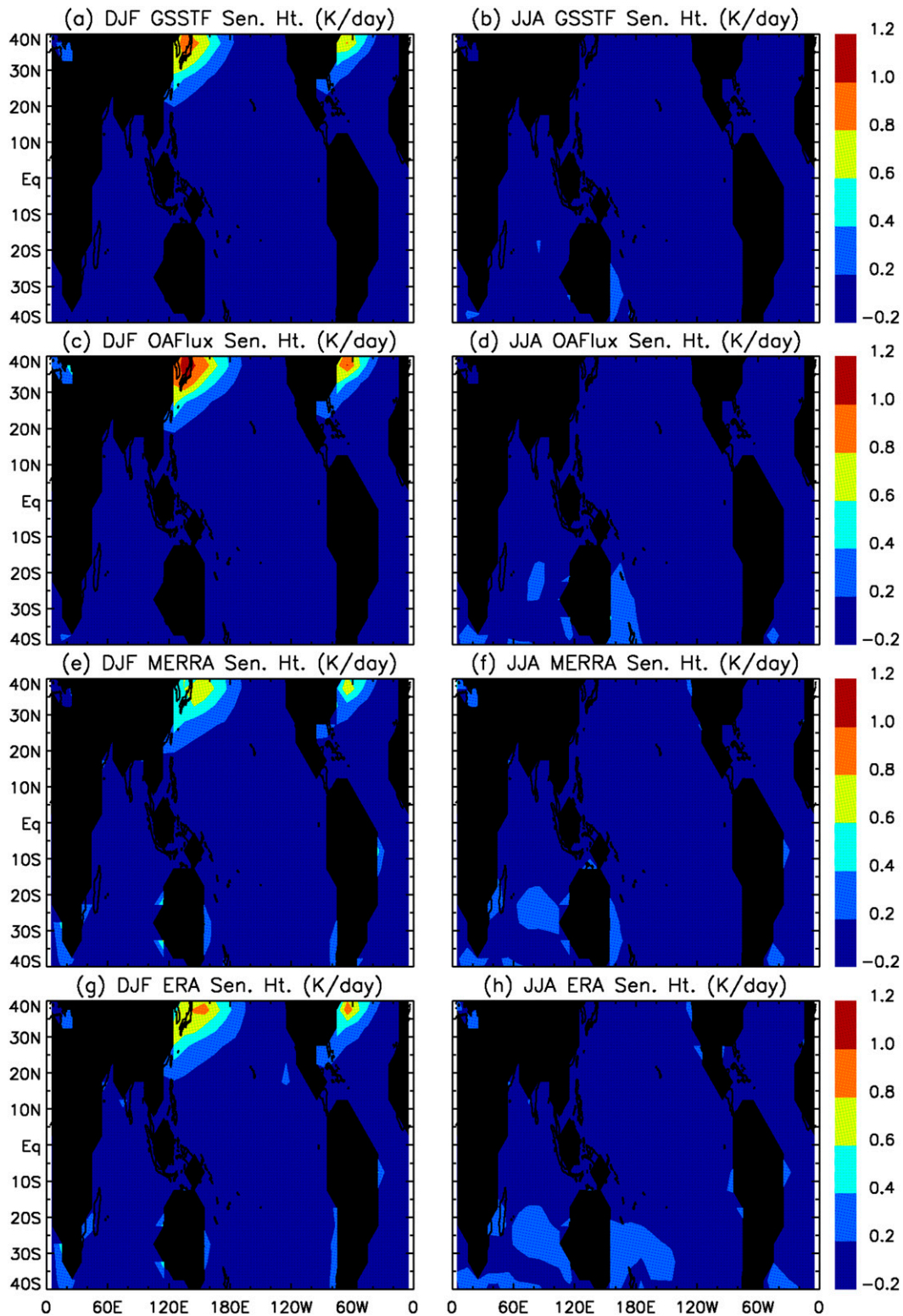
FIG. 4. Surface sensible heat fluxes from (a),(b) GSSTF2c; (c),(d) OAFlux; and (e),(f) MERRA: (left) seasonal averages for DJF in 2004–07 and (right) the averages for JJA for the same years. The units are converted to kelvin per day by assuming an atmospheric layer thickness of 70–1000 hPa. The black area shows regions with missing data or with land cover greater than 50%.
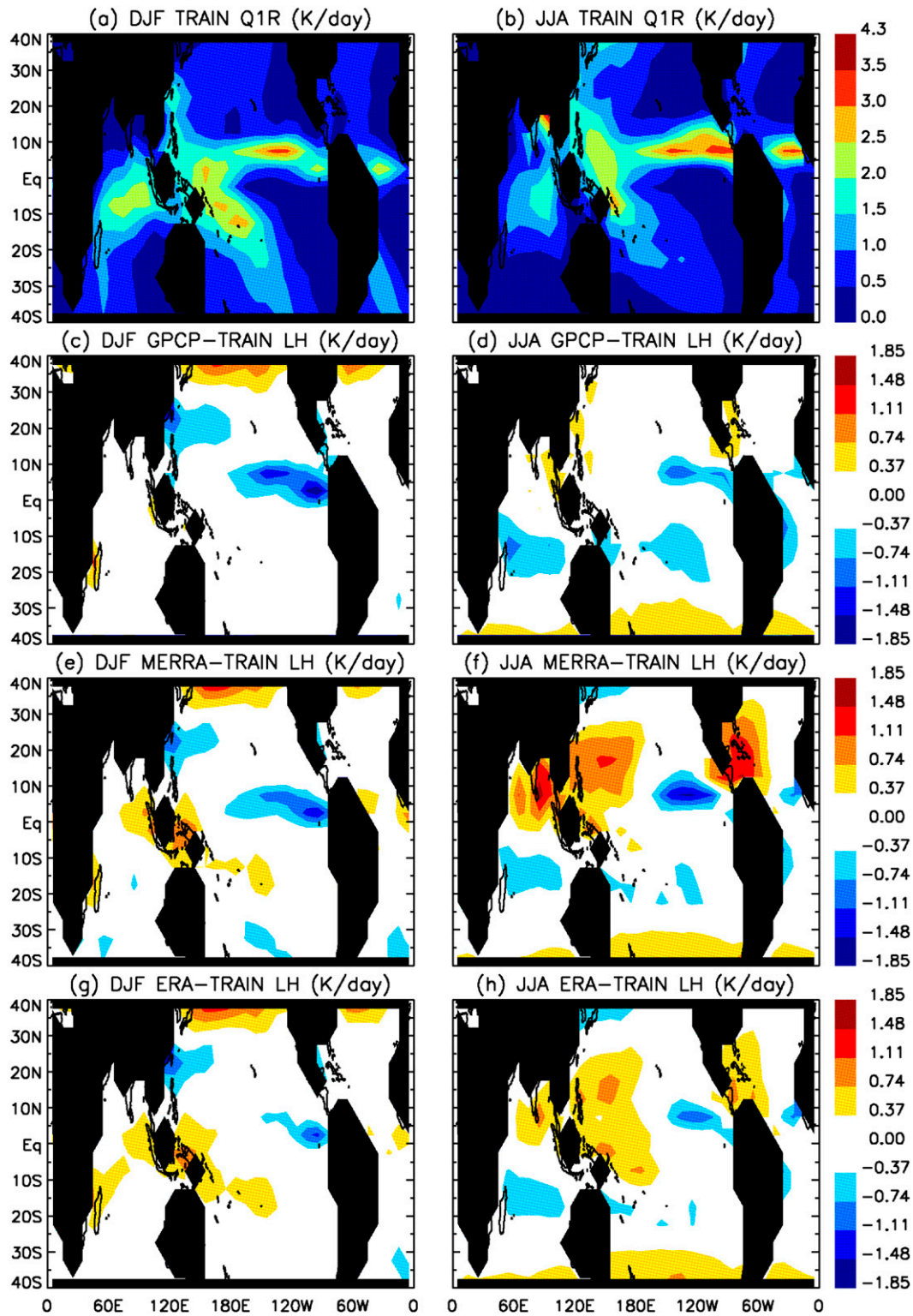
FIG. 5. (a),(b) Column-integrated latent heating rates (K day^{-1}) calculated from TRAIN Q1R. Differences, from TRAIN Q1R, in the column-integrated latent heating rates of (c),(d) GPCP 1DD precipitation and the (e),(f) MERRA and (g),(h) ERA-Interim precipitation: (left) the seasonal averages for DJF in 2004–07 and (right) the averages for JJA in the same years. For (c)–(h), the contour interval is the 1σ uncertainty of the TRAIN QR. The black area shows regions with missing data or with land cover greater than 50%.
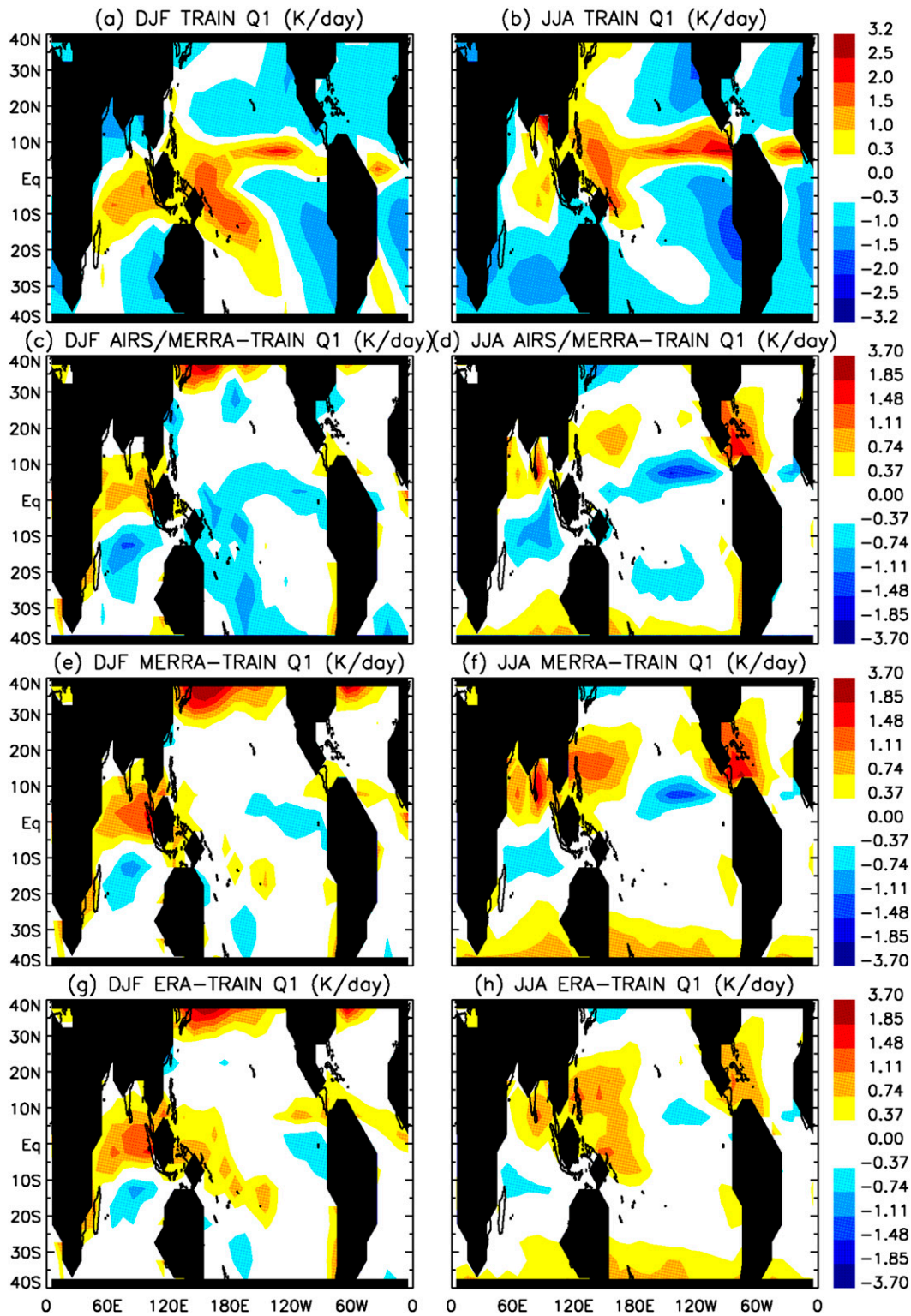
FIG. 6. (a),(b) Column-integrated atmospheric diabatic heating rates ($K\,day^{-1}$) calculated from TRAIN Q1. Differences, from TRAIN Q1, in the atmospheric diabatic heating rates of (c),(d) AIRS/MERRA Q1; (e),(f) MERRA Q1; and (g),(h) ERA-Interim Q1: (left) the seasonal averages for DJF in 2004–07 and (right) the averages for JJA in the same years. For (c)–(h), contour interval is the 1σ uncertainty of the TRAIN QR except the last interval, which is from 5σ to 10σ. The black area shows regions with missing data or with land cover greater than 50%.
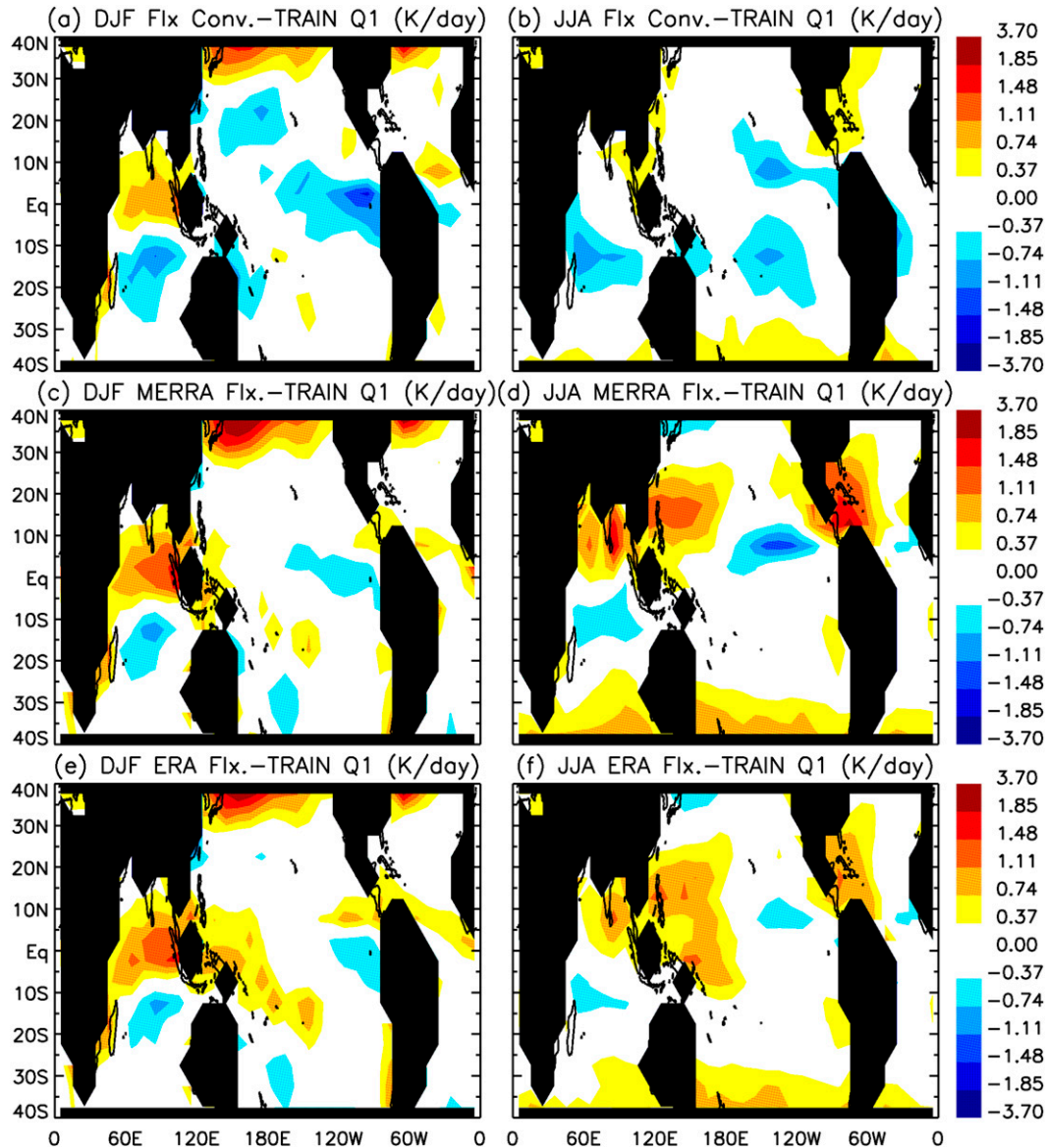
FIG. 7. Differences, from TRAIN Q1, in heat flux convergence (K day^{-1}) between the TOA (at 70 hPa) and the surface calculated from (a),(b) SRB radiative fluxes, GSSTF2c surface sensible fluxes, and the GPCP precipitation as well as from (c),(d) the MERRA and (e),(f) ERA-Interim heat fluxes and precipitation: (left) the seasonal averages for DJF in 2004–07 and (right) the averages for JJA for the same years. Contour interval is the 1σ uncertainty of the TRAIN QR except the last interval, which is from 5σ to 10σ. The black area shows regions with missing data or with land cover greater than 50%.

heating rates at annual and semiannual time scales. Intraseasonal variations in total heating rates are mainly contributed from the variations in latent heating.

The tropical Atlantic has strong semiannual variability in total heating rates (Fig. 13, top). All datasets have similar patterns of wavelet spectra of the total heating rates. TRAIN Q1, AIRS/MERRA Q1, MERRA and ERA Q1, and FLUX CONV all show a distinct peak of semiannual signal in early 2006. For the variations

in radiative heating (Fig. 13, middle), TRAIN Q1 and ERA-Interim has semiannual amplitude ($\sim$0.4–0.5 K day^{-1}) larger than the annual amplitude, while the MERRA and the SRB FLUX CONV have larger annual amplitudes ($\sim$0.5–0.6 K day^{-1}) than the semiannual amplitudes. The variation in latent heating is about 3–4 times larger than that in radiative heating in this region (Fig. 13, middle and bottom). TRAIN Q1R and GPCP 1DD precipitation (Fig. 13, bottom) show
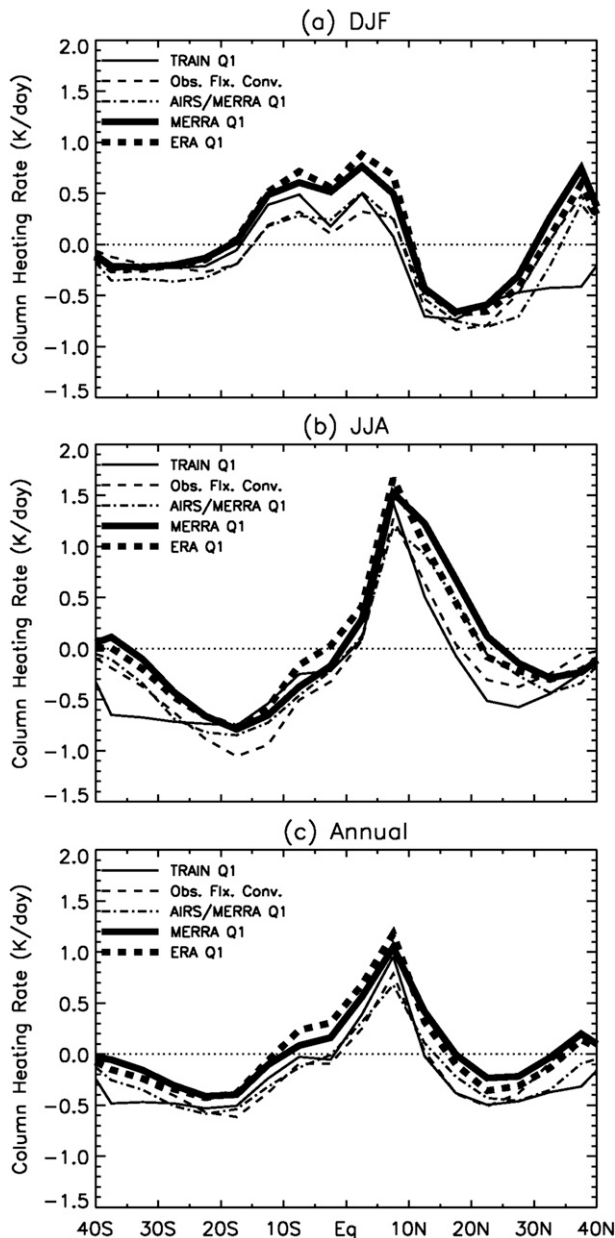
FIG. 8. Zonal mean column-integrated heating rates (K day^{-1}) estimated from several datasets for the (a) winter (DJF), (b) summer (JJA), and (c) annual averages. The zonal mean is taken for area with land cover less than 50%. The thin solid lines show the heating rates from TRAIN Q1; the thin dashed lines show the rates from AIRS/MERRA Q1; the thin dashed–dotted lines show the rates from MERRA Q1; the thick dashed–dotted lines show the rates calculated from the convergence of MERRA heat fluxes and precipitation; and the thick dashed lines show the rates estimated from the convergence of SRB fluxes, GSSTF2c sensible heat fluxes, and GPCP 1DD precipitation.

comparable annual and semiannual amplitudes in latent heating ($\sim$1.5–2.3 K day^{-1}), while the MERRA and ERA Q1 show semiannual amplitude ($\sim$2–2.3 K day^{-1}) larger than the annual amplitude ($\sim$1.3–1.5 K day^{-1}).
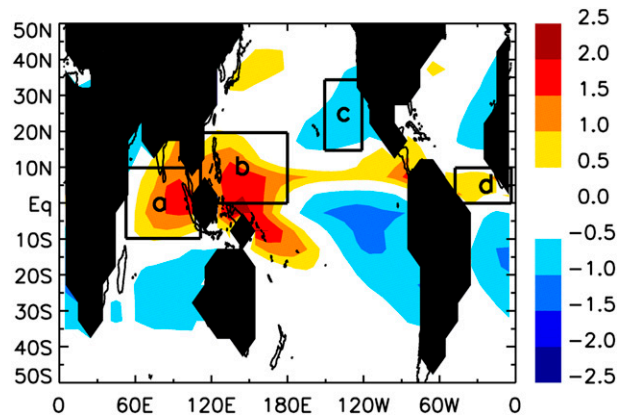
FIG. 9. Regions for averaging Q1 or energy flux convergence for wavelet analyses shown in Figs. 10–12. The regions are denoted as tropical Indian Ocean (box a:10°S–10°N, 50°–110°E), west Pacific (box b: 0°–20°N, 110°E–180°), northeast Pacific (box c: 15°–35°N, 150°–120°W), and tropical Atlantic (box d: 0°–10°N, 45°W–0°). Color contours indicate the annual-mean energy flux convergence from the MERRA for 2004–07.

4. Conclusions and discussion

Atmospheric energy balance and the variability of diabatic heating rates are investigated using different satellite-based observations over the oceans in 40°S–40°N. The atmospheric heating rates (TRAIN Q1) are calculated as the sum of radiative heating (QR) and latent heating (Q1R) based on the TRMM measurements. Independent estimates of atmospheric heating rates (AIRS/MERRA Q1) are derived from the AIRS L3 temperatures and MERRA wind fields. The column integrals of these atmospheric heating rates are compared to the heat flux convergence calculated from independent datasets of heat fluxes at the TOA and the surface. Shortwave and longwave radiative heat fluxes are obtained from the SRB, while the surface sensible heat flux is obtained from either the GSSTF2c or the OAFlux. Latent heat fluxes from the surface do not influence atmospheric energy budget locally but contribute to atmospheric heating where water vapor condenses and precipitates. Therefore, the heat flux should include latent heating, for which the precipitation syntheses of the GPCP 1DD are used. In addition to the satellite-based estimates, we investigate heating rates and heat fluxes from MERRA and ERA-Interim.

All datasets reproduce reasonable seasonal climatologies of atmospheric heating patterns that include the heating in the intertropical convergence zone (ITCZ), the tropical western Pacific, and the summertime monsoons, as well as the cooling in the subtropical oceans. There are detailed quantitative discrepancies among datasets that can be categorized into two climate regimes: 1) the
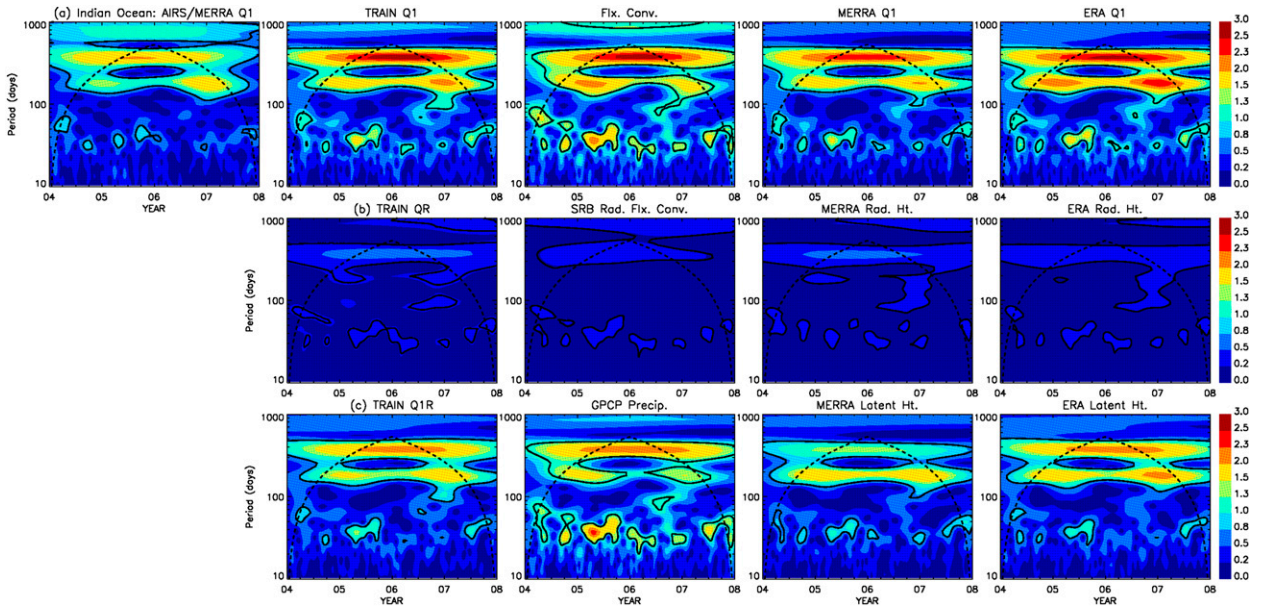
FIG. 10. (top) Wavelet spectra of the averaged total heating rates over the tropical Indian Ocean (box a in Fig. 9) from AIRS/MERRA Q1, MERRA Q1, MERRA energy flux convergence, and energy flux convergence from observation-based syntheses. (middle) Wavelet spectra of the radiative heating rates for the TRAIN, MERRA radiative heating, MERRA radiative flux convergence, and the SRB flux convergence. (bottom) Wavelet spectra of latent heating rates for the TRAIN, MERRA latent heating, MERRA precipitation, and GPCP 1DD precipitation. The unit of the amplitudes are kelvin per day. The dashed lines indicate the regimes influenced by the edge effect; the solid lines circle ,the regime with a 95% confidence level.

regime where thick clouds and heavy precipitations occur frequently and 2) the subtropical oceans where subsidence occurs and radiative cooling dominates over the local energy budget.

In the summertime monsoon area and tropical western Pacific, the reanalyses have the largest atmospheric heating rates (Figs. 6 and 7) because they have the largest local latent heating (Fig. 5). In the ITCZ of tropical eastern Pacific, TRAIN Q1 has the largest latent heating. Larger cloud radiative forcing in MERRA and ERA-Interim compared to TRAIN QR (Fig. 3) is evident in its smaller surface net downward radiation.
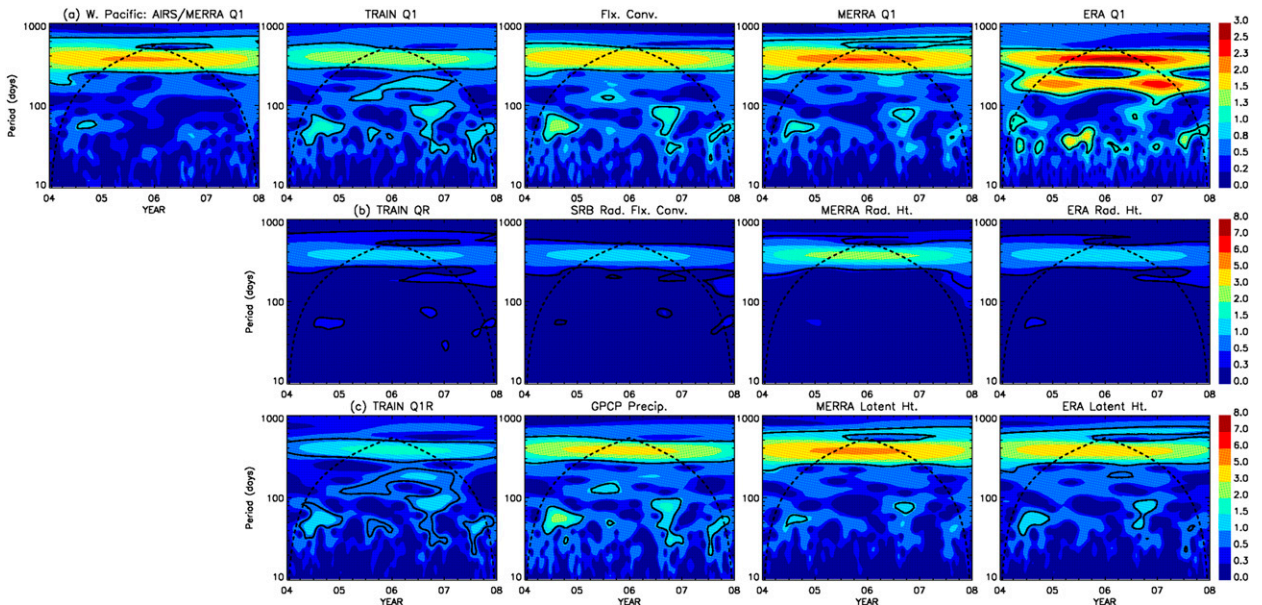

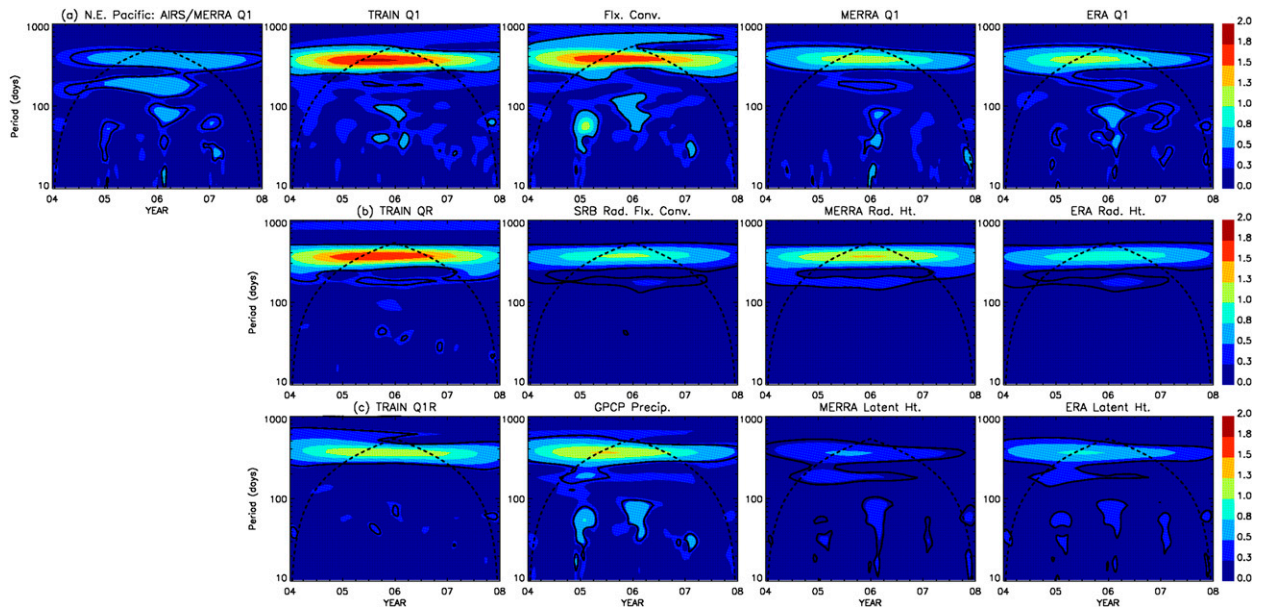FIG. 11. As in Fig. 10, but for the west Pacific (box b in Fig. 9).

FIG. 12. As in Fig. 10, but for the northeast Pacific (box c in Fig. 9).

Compared to the reanalyses, AIRS/MERRA Q1 tends to underestimate atmospheric heating rates in these regions because of the sampling bias in the AIRS temperature in cloudy conditions.

In the subtropical oceans where latent heat plays a relatively minor role in the atmospheric heat budget climatology, TRAIN QR has stronger radiative cooling rates compared to the reanalysis cooling rates (Fig. 3). This is mainly caused by the significantly larger surface downward longwave radiative flux in HERB (not shown). As the uncertainty in the HERB downward shortwave radiative fluxes is large ($34 \, \mathrm{W \, m^{-2}}$), the significant difference of the HERB downward longwave radiative flux at the subtropical ocean surface from the other datasets is masked in the total surface heat flux plots (Fig. 2). In fact, the TRAIN Q1 larger net cooling rates over the subtropical oceans, compared to other datasets, are mainly contributed by its large downward longwave flux at the surface.

The discrepancies described above manifest themselves in globally averaged heat budgets over the oceans
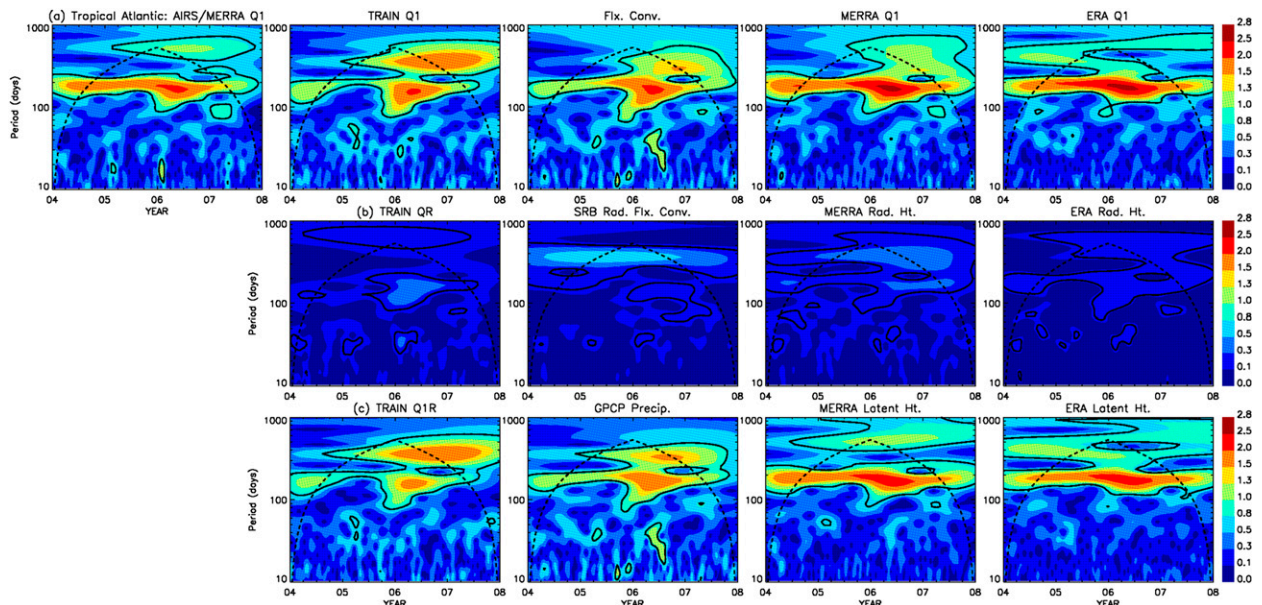

FIG. 13. As in Fig. 10, but for the tropical Atlantic (box d in Fig. 9).

(Table 4). Over the oceans in 40°S–40°N, the smaller radiative heating in cloudy areas and the stronger radiative cooling over the subtropical oceans in HERB result in the most negative averaged radiative heating rate ($-122\,\mathrm{W\,m^{-2}}$) compared to the other datasets (from -112 to $-116\,\mathrm{W\,m^{-2}}$). The reanalyses have the largest latent heating rates ($\sim100\,\mathrm{W\,m^{-2}}$) compared to the observation-based datasets ($88–90\,\mathrm{W\,m^{-2}}$) because of their large latent heating over regions with active convection. Sensible heating rates averaged over tropical oceans range from 8 to $15\,\mathrm{W\,m^{-2}}$. Regarding the total heating rates, AIRS/MERRA Q1 and TRAIN Q1 tend to lie at the lower end of the range of the estimates. AIRS temperatures have cold biases over thick clouds or heavy precipitating area that cause the underestimate of total heating rates in AIRS/MERRA Q1 when compared to the reanalyses. However, the uncertainties in reanalysis winds may also influence the AIRS/MERRA Q1 and make it difficult to diagnose the origin of its difference from other observation-based products.

The discrepancy between the reanlaysis net heating rates and the observation-based estimates is larger than the 1σ spread of the observation-based estimates. This discrepancy implies different pictures of global atmospheric heat transport. Large sensible heating over land between 40°S and 40°N provides a main heat source of the atmosphere in low latitudes. In observation-based products, net atmospheric cooling over the oceans in low latitudes implies a picture of atmospheric heat transport from the low-latitude land to the low-latitude ocean as well as to high latitudes. However, in the reanalyses, net atmospheric warming over the oceans in low latitudes implies a picture of simple poleward heat transport in the atmosphere. This discrepancy of atmospheric heat transport between the observation-based and reanalysis datasets need further investigation.

Temporal variability of total atmospheric heating rates over regions along the ITCZ and subtropical oceans is also investigated. Wavelet spectra of total heating rates based upon different estimates (averaged over the selected regions in Fig. 9) have similar patterns (Figs. 10a–13a), showing maxima of variability in annual, semiannual, and intraseasonal time scales. In climate regimes where precipitation occurs frequently, such as the tropical Indian Ocean; the tropical western, eastern, and South Pacific; and the tropical Atlantic, the total heating rate variations are mainly driven by variations in latent heating. Over the subtropical oceans, where radiative cooling dominates in the climatological total heating rate, both radiative and latent heating contribute significantly to the annual and semiannual cycles of the total heating rates, while latent heating is important in generating the heating variability at intraseasonal time scales.

Wavelet spectra of radiative latent heating rates may show qualitative differences in the patterns, depending on the region being investigated. For instance, the wavelet spectrum of atmospheric radiative heating of the SRB over the tropical Indian Ocean has much smaller semiannual variation than that of TRAIN QR and the reanalyses. On the other hand, the wavelet spectrum of radiative heating from TRAIN QR and ERA-Interim over the tropical Atlantic has much smaller annual variations compared to those in the SRB and MERRA.

The local-balance study presented here could be used as a test of the satellite retrieval data and the reanalyses with regard to its ability to faithfully represent important climate processes. The study is highly relevant to Joint Polar Satellite System (JPSS) (Lee et al. 2010) Cross-Track Infrared and Advanced Technology Microwave Sounder Suite (CrIMSS) observations. Regarding estimation of precipitation and latent heating, the NASA–Japan Aerospace Exploration Agency (JAXA) Global Precipitation Measurement (GPM) mission is expected to continue and expand upon the spaceborne radar/passive microwave record that TRMM has provided (1998–present) and expand the area coverage to higher latitudes. Furthermore, continuity could be established with AIRS and JPSS as well as with TRMM and GPM to quantify long-term behavior in trends and variability of heating rates with climate change.

REFERENCES

Behrangi, A., M. Lebsock, S. Wong, and B. Lambrigtsen, 2012: On the quantification of oceanic rainfall using spaceborne sensors. *J. Geophys. Res.,* **117,** D20105, doi:10.1029/2012JD017979.

Berg, W., T. L'Ecuyer, and J. M. Haynes, 2010: The distribution of rainfall over oceans from spaceborne radars. *J. Appl. Meteor.,* **49,** 535–543.

Bosilovich, M. G., F. R. Robertson, and J. Chen, 2011: Global energy and water budgets in MERRA. *J. Climate,* **24,** 5721–5739.

Brunke, M. A., Z. Wang, X. Zeng, M. Bosilovich, and C.-L. Shie, 2011: An assessment of the uncertainties in ocean surface turbulent fluxes in 11 reanalysis, satellite-derived, and combined global datasets. *J. Climate,* **24,** 5469–5493.

Chou, S.-H., E. Nelkin, J. Ardizzone, R. M. Atlas, and C.-L. Shie, 2003: Surface turbulent heat and momentum fluxes over global oceans based on the Goddard satellite retrieval, version 2 (GSSTF2). *J. Climate,* **16,** 3256–3273.

Cooper, S. J., T. S. L'Ecuyer, and G. L. Stephens, 2003: The impact of explicit cloud boundary information on ice cloud microphysical property retrievals from infrared radiances. *J. Geophys. Res.,* **108,** 4107, doi:10.1029/2002JD002611.

Dee, D. P., and Coauthors, 2011: The ERA-Interim reanalysis: Configuration and performance of the data assimilation system. *Quart. J. Roy. Meteor. Soc.,* **137,** 553–597, doi:10.1002/qj.828.

Divakarla, M. G., C. D. Barnet, M. D. Goldberg, L. M. McMillin, E. Maddy, W. Wolf, L. Zhou, and X. Liu, 2006: Validation of AIRS temperature and water vapor retrievals with matched radiosonde measurements and forecasts. *J. Geophys. Res.,* **111,** D09S15, doi:10.1029/2005JD006116.

Farge, M., 1992: Wavelet transforms and their application to turbulence. *Annu. Rev. Fluid Mech.,* **24,** 395–457.

Fetzer, E. J., J. Teixeira, E. T. Olsen, and E. F. Fishbein, 2004: Satellite remote sounding of atmospheric boundary layer temperature inversions over the subtropical eastern Pacific. *Geophys. Res. Lett.,* **31,** L17102, doi:10.1029/2004GL020174.

——, B. H. Lambrigtsen, A. Eldering, H. H. Aumann, and M. T. Chahine, 2006: Biases in total precipitable water vapor climatologies from Atmospheric Infrared Sounder and Advanced Microwave Scanning Radiometer. *J. Geophys. Res.,* **111,** D09S16, doi:10.1029/2005JD006598.

Fu, Q., K. N. Liou, M. C. Cribb, T. P. Charlock, and A. Grossman, 1997: Multiple scattering parameterization in thermal infrared radiative transfer. *J. Atmos. Sci.,* **54,** 2799–2812.

Grecu, M., and W. S. Olson, 2006: Bayesian estimation of precipitation from satellite passive microwave observations using combined radar–radiometer retrievals. *J. Appl. Meteor. Climatol.,* **45,** 416–433.

——, ——, C. L. Shie, T. S. L'Ecuyer, and W. K. Tao, 2009: Combining satellite microwave radiometer and radar observations to estimate atmospheric heating profiles. *J. Climate,* **22,** 6356–6376.

Greenwald, T. J., G. L. Stephens, T. H. Vonder Haar, and D. L. Jackson, 1993: A physical retrieval of cloud liquid water over the global oceans using Special Sensor Microwave/Imager (SSM/I) observations. *J. Geophys. Res.,* **98,** 18 471–18 488.

Gupta, S. K., W. L. Darnell, and A. C. Wilber, 1992: A parameterization for longwave surface radiation from satellite data: Recent improvements. *J. Appl. Meteor.,* **31,** 1361–1367.

——, D. P. Kratz, P. W. Stackhouse Jr., and A. C. Wilber, 2001: The Langley parameterized shortwave algorithm (LPSA) for surface radiation budget studies. NASA Tech. Rep. NASA/TP-20010211272, 31 pp.

Huffman, G. J., R. F. Adler, M. Morrissev, D. T. Bolvin, S. Curtis, R. Joyce, B. McGavock, and J. Susskind, 2001: Global precipitation at one-degree daily resolution from multi-satellite observations. *J. Hydrometeor.,* **2,** 36–50.

——, ——, D. T. Bolvin, and G. Gu, 2009: Improving the global precipitation record: GPCP version 2.1. *Geophys. Res. Lett.,* **36,** L17808, doi:10.1029/2009GL040000.

Kalnay, E., and Coauthors, 1996: The NCEP/NCAR 40-Year Reanalysis Project. *Bull. Amer. Meteor. Soc.,* **77,** 437–471.

L'Ecuyer, T. S., and G. L. Stephens, 2003: The tropical atmospheric energy budget from the TRMM perspective. Part I: Algorithm and uncertainties. *J. Climate,* **16,** 1967–1985.

——, and ——, 2007: The tropical atmospheric energy budget from the TRMM perspective. Part II: Evaluating GCM representations of the sensitivity of regional energy and water cycles to the 1998–99 ENSO cycle. *J. Climate,* **20,** 4548–4571.

——, and G. McGarragh, 2010: A 10-year climatology of atmospheric radiative heating and its vertical structure from TRMM observations. *J. Climate,* **23,** 519–541.

Lee, T. F., and Coauthors, 2010: NPOESS: Next-Generation Operational Global Earth Observations. *Bull. Amer. Meteor. Soc.,* **91,** 727–740.

Lin, B., P. W. Stackhouse Jr., P. Minnis, B. A. Wielicki, Y. Hu, W. Sun, T.-F. Fan, and L. M. Hinkelman, 2008: Assessment of global annual atmospheric energy balance from satellite observations. *J. Geophys. Res.,* **113,** D16114, doi:10.1029/2008JD009869.

Olsen, E. T., S. Granger, E. Manning, and J. Blaisdell, 2007: AIRS/AMSU/HSB version 5 level 3 quick start: Version 1.1. Jet Propulsion Laboratory/California Institute of Technology Rep., 25 pp.

Peixoto, J. P., and A. H. Oort, 1992: *Physics of Climate.* American Institute of Physics, 520 pp.

Pinker, R. T., and I. Laszlo, 1992: Modeling surface solar irradiance for satellite applications on a global scale. *J. Appl. Meteor.,* **31,** 194–211.

Rienecker, M. M., and Coauthors, 2008: The GEOS-5 Data Assimilation System—Document of versions 5.0.1, 5.1.0, and 5.2.0. NASA Global Modeling and Data Assimilation Tech. Rep. 27, 188 pp.

——, and Coauthors, 2011: MERRA: NASA's Modern-era retrospective analysis for research and applications. *J. Climate,* **24,** 3624–3648.

Saha, S., and Coauthors, 2010: The NCEP Climate Forecast System Reanalysis. *Bull. Amer. Meteor. Soc.,* **91,** 1015–1057.

Schumacher, C., P. E. Ciesielski, and M. H. Zhang, 2008: Tropical cloud heating profiles: Analysis from KWAJEX. *Mon. Wea. Rev.,* **136,** 4289–4300.

Shie, C.-L., 2011: Science background for the reprocessing and Goddard Satellite-based Surface Turbulent Fluxes (GSSTF2c) dataset for global water and energy cycle research. Goddard Earth Sciences (GES) Data and Information Services Center Rep., 19 pp. [Available online at http://disc.sci.gsfc.nasa.gov/measures/documentation/Science_of_the_data.GSSTF2c.pdf.]

——, and Coauthors, 2009: A note on reviving the Goddard Satellite-based Surface Turbulent Fluxes (GSSTF) dataset. *Adv. Atmos. Sci.,* **26,** 1071–1080.

——, K. Hilburn, L. S. Chiu, R. Adler, I.-I. Lin, E. Nelkin, and J. Ardizzone, cited 2011: The Goddard Satellite-based Surface Turbulent Fluxes dataset–version 2c (GSSTF2c): Global (grid of 1° × 1°) daily air-sea surface fluxes from July 1987 to December 2008. Goddard Earth Sciences (GES) Data and Information Services Center. [Available online at http://disc.sci.gsfc.nasa.gov/daac-bin/DataHoldingsMEASURES.pl?PROGRAM_List=ChungLinShie.]

Shige, S., Y. N. Takayabu, and W.-K. Tao, 2008: Spectral retrieval of latent heating profiles from TRMM PR data. Part III: Estimating apparent moisture sink profiles over tropical oceans. *J. Appl. Meteor. Climatol.,* **47,** 620–640.

Stackhouse, P. W., Jr., S. K. Gupta, S. J. Cox, T. Zhang, J. C. Mikovitz, and L. M. Hinkelman, 2011: The NASA/GEWEX surface radiation budget release 3.0: 24.5-year dataset. *GEWEX News,* No. 21, International GEWEX Project Office, Silver Spring, MD, 10–12.

Stephens, G. L., and Coauthors, 2012a: An update on Earth's energy balance in light of the latest global observations. *Nat. Geosci.,* **5,** 691–696.

——, M. Wild, P. W. Stackhouse Jr., T. L'Ecuyer, S. Kato, and D. S. Henderson, 2012b: The global character of the flux of downward longwave radiation. *J. Climate,* **25,** 2329–2340.

Susskind, J., C. Barnet, J. Blisdell, L. Iredell, F. Keita, L. Kouvaris, G. Molnar, and M. Chahine, 2006: Accuracy of geophysical parameters derived from Atmospheric Infrared Sounder/Advanced Microwave Sound Unit as a function of fractional cloud cover. *J. Geophys. Res.,* **111,** D09S17, doi:10.1029/2005JD006272.

Trenberth, K. E., J. T. Fasullo, and J. Kiehl, 2009: Earth's global energy budget. *Bull. Amer. Meteor. Soc.,* **90,** 311–323.

——, ——, and J. Mackaro, 2011: Atmospheric moisture transports from ocean to land and global energy flows in reanalyses. *J. Climate,* **24,** 4908–4924.

Wong, S., E. J. Fetzer, B. H. Kahn, B. Tian, B. H. Lambrigtsen, and H. Ye, 2011a: Closing the global water vapor budget with AIRS water vapor, MERRA reanalysis, TRMM and GPCP precipitation, and GSSTF surface evaporation. *J. Climate,* **24,** 6307–6321.

——, ——, B. Tian, B. Lambrigtsen, and H. Ye, 2011b: The apparent water vapor sinks and heat sources associated with the intraseasonal oscillation of the Indian summer monsoon. *J. Climate,* **24,** 4466–4479.

Yanai, M., S. Esbensen, and J.-H. Chu, 1973: Determination of bulk properties of tropical cloud clusters from large-scale heat and moisture budgets. *J. Atmos. Sci.,* **30,** 611–627.

Yu, L., and R. A. Weller, 2007: Objectively analyzed air–sea heat fluxes for the global ice-free oceans (1981–2005). *Bull. Amer. Meteor. Soc.,* **88,** 527–539.

Yue, Q., E. J. Fetzer, B. H. Kahn, S. Wong, G. Manipon, A. Guillaume, and B. Wilson, 2013: Cloud-state-dependent sampling in AIRS observations based on *CloudSat* cloud classification. *J. Climate,* **26,** 8357–8377.

Zhang, Y., W. B. Rossow, A. A. Lacis, V. Oinas, and M. I. Mishchenko, 2004: Calculation of radiative fluxes from the surface to top of atmosphere based on ISCCP and other global data sets: Refinements of the radiative transfer model and the input data. *J. Geophys. Res.,* **109,** D10105, doi:10.1029/2003JD004457.

——, ——, and P. W. Stackhouse Jr., 2006: Comparison of different global information sources used in surface radiative flux calculation: Radiative properties of the surface. *J. Geophys. Res.,* **111,** D13106, doi:10.1029/2005JD006873.